Journal of Marine Science and Technology

Volume 26 | Issue 1 Article 7

AN APPROACH TO ALIGNING REGIONS OF INTEREST ON INFRARED PALM-DORSUM IMAGES CAPTURED IN CONTACTLESS SCENARIOS

Chih-Lung Lin
Department of Electronic Engineering, Hwa Hsia University of Technology, New Taipei City, Taiwan, R.O.C Department of Information and Computer Engineering, Chung Yuan ChristianUniversity, Taoyuan City, Taiwan, R.O.C,
linclr@gmail.com

Hui-Fen Chiang
Department of Digital Multimedia Design, Taipei City University of Science and Technology, Taipei City, Taiwan, R.O.C. 4 Department of Computer Science and Engineering, National Taiwan Ocean University, Keelung City, Taiwan, R.O.C

Hsu-Yung Cheng
Department of Computer Science and Information Engineering, National Central University, Taoyuan City, Taiwan, R.O.C

Chih-Wei Kuo
Materials & Electro-Optics Research Division, National Chung-Shan Institute of Science & Technology, Taoyuan City, Taiwan, R.O.C. Department of Electro-Optical Engineering, National United University, Miaoli County, Taiwan, R.O.C.

Jun-Wei Hsieh
Department of Computer Science and Engineering, National Taiwan Ocean University, Keelung City, Taiwan, R.O.C.

AN APPROACH TO ALIGNING REGIONS OF INTEREST ON INFRARED PALM-DORSUM IMAGES CAPTURED IN CONTACTLESS SCENARIOS

Acknowledgements

The authors would like to acknowledge the support for this study through grants from National Chung-Shan Institute of Science & Technology (NCSIST-442-V301 (106)) and Ministry of Science and Technology (MOST 106-2221-E-146-007). They would also thank the anonymous reviewers for their significant and constructive critiques and suggestions, which substantially improved the quality of this paper.

Journal of Marine Science and Technology, Vol. 26, No. 1, pp. 73-83 (2018)
DOI: 10.6119/JMST.2018.02_(1).0010

AN APPROACH TO ALIGNING REGIONS OF INTEREST ON INFRARED PALM-DORSUM IMAGES CAPTURED IN CONTACTLESS SCENARIOS

Chih-Lung Lin[1, 2], Hui-Fen Chiang[3, 4], Hsu-Yung Cheng[5], Chih-Wei Kuo[6, 7], and Jun-Wei Hsieh[4]

Key words: hand-based biometrics, palmprint, vein-pattern, regions of interest, affine transformation.

ABSTRACT

This paper presents an approach for solving a highly challenging problem in the preprocessing of hand-based biometrics, namely restoring IR palm-dorsum images captured in contactless scenarios and aligning regions of interest (ROIs) in the same regions on the various restored infrared (IR) palm-dorsum images captured from the same palm-dorsum. IR palm-dorsum images captured in contactless scenarios substantially increase the user-friendliness, security and sanitation of hand-based biometrics. However, images captured in contactless scenarios typically exhibit rotation, translation, scale and shear geometric transformations. These geometric transformations significantly reduce the accuracy of hand-based biometrics. An approach used to restore and align ROI on an IR palm-dorsum image is proposed to solve this problem. The proposed approach is based on a two-dimensional affine image transformation scheme used to restore the geometric transformations of the images, and an ROI alignment method based on finger-web positions. Thus, the proposed approach improves the user-friendliness, security, sanitation and accuracy of hand-based biometrics based on features extracted from the ROI. The principal characteristics of the proposed approach are no prior information on IR images being necessary, and no parameters being required to be preset. The experimental results indicated the effectiveness and feasibility of the proposed approach. The proposed approach improves accuracy, user-friendliness, security and sanitation and extends the application of hand-based biometrics for use in security access control systems.

I. INTRODUCTION

Because of handheld mobile devices, cloud computing, and the Internet have been growing immensely in use and appeal in daily life. The need for security assurance and privacy protection has rapidly increased in recent years. Biometrics is an effective solution to security assurance and privacy protection problems. Several biometric techniques, such as hand-based, facial, iris pattern, retina pattern (Sanchez-Reillo et al., 2000), voice, signature, and gesture recognition, have been proposed for improving security and privacy. Hand-based biometrics is a widely used biometric technology. Hand-based biometrics is based on various techniques including fingerprint, palmprint, palm geometry, palm shape, finger-knuckle print, and palm vein-pattern recognition.

Numerous challenges remain regarding improving the accuracy, security, sanitation and user-friendliness of hand-based biometric techniques. To increase identification accuracy and reliability, the features extracted from the same region of various palm images are compared. The region to be extracted is known as the regions of interest (ROI). Most hand-based biometric technologies compare the features extracted from the ROI in different palm images. Adjusting the ROI to be aligned in the same position in various palm images is critical to ensure the stability of the extracted features. However, adjusting the ROI to be aligned at the same position in various palm images is difficult without using fixed pegs to constrain the palm position.

Paper submitted 04/27/15; revised 10/17/16; accepted 09/06/17. Author for correspondence: Chih-Lung Lin (e-mail: linclr@gmail.com).
[1] *Department of Electronic Engineering, Hwa Hsia University of Technology, New Taipei City, Taiwan, R.O.C.*
[2] *Department of Information and Computer Engineering, Chung Yuan Christian University, Taoyuan City, Taiwan, R.O.C.*
[3] *Department of Digital Multimedia Design, Taipei City University of Science and Technology, Taipei City, Taiwan, R.O.C.*
[4] *Department of Computer Science and Engineering, National Taiwan Ocean University, Keelung City, Taiwan, R.O.C.*
[5] *Department of Computer Science and Information Engineering, National Central University, Taoyuan City, Taiwan, R.O.C.*
[6] *Materials & Electro-Optics Research Division, National Chung-Shan Institute of Science & Technology, Taoyuan City, Taiwan, R.O.C.*
[7] *Department of Electro-Optical Engineering, National United University, Miaoli County, Taiwan, R.O.C.*

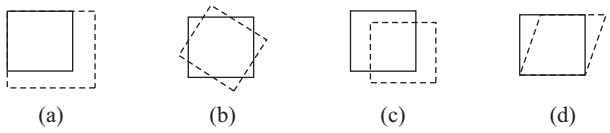

Fig. 1. Shows the schematic diagrams of geometric transformations. Graphs with black solid line are the original graphs. Graphs with blue dashed line show the geometric transformations. (a) scale, (b) rotation, (c) translation, (d) shear.

Several techniques used for personal identification based on hand-based features have been proposed in the literature. To use these techniques, users must place their palms on a flat surface and be constrained by fixed pegs to minimize movement of their palm position (Jain et al., 1999; Jain et al., 1999; Elliott et al., 2010; Sanchez-Reillo et al., 2000). These constraints facilitate the feature extraction procedure and yield a high accuracy rating; however, such systems are not user-friendly.

To circumvent this problem, a few researchers have proposed approaches to capturing palm images without necessitating fixed pegs to constrain the palm position (Lin et al., 2005; Xiong et al., 2005; Yörük et al., 2006; Dutagaci et al., 2008; Kumar and Ravikanth, 2009; Lin et al., 2013; Raghavendra et al., 2014) while capturing the palm images. The ROI alignment algorithm incorporated in the proposed approaches resolves the possible rotation or translation geometric transformations of palm images captured without the need for any fixed pegs. However, users are still required to place their palms on a digital scanner or flat surface. Such contact might induce sanitation or security concerns of users.

A security concern of contact-based approaches is the possibility of picking up fingerprint or palmprint impressions left on the flat surface by a user. The aim of implementing contactless hand-based biometrics is to mitigate the increasing sanitation and security concerns and make it user-friendly.

Because palms have a high degree of pose variability, palm images captured in contactless scenarios typically exhibit rotation, translation, scale and shear geometric transformations as shown in Fig. 1. The geometric transformations reduce the accuracy of hand-based biometrics.

Accurately restoring the geometric transformations of an image is a crucial and challenging task for contactless hand-based biometric applications. Several studies (Jiang et al., 2007; Morales et al., 2008; Zheng et al., 2007; de-Santos-Sierra et al., 2011; Zhou and Kumar, 2011) on contactless hand-based biometric schemes have been conducted; however, these studies have not considered restoring geometric transformations of palm images captured in contactless scenarios. Only Zheng et al. (2007) and Zhou and Kumar (2011) have discussed mitigating the influences of geometric transformations. Zheng et al. (2007) applied projective-invariant features to alleviate the influences of the geometric transformations of palm images. Zhou and Kumar (2011) used an ROI normalization scheme to reduce the influences of the geometric transformations of palm images.

Infrared (IR) images have frequently been used in identification applications, such as vein-pattern identification (Cross and Smith, 1995; Prokoski, 2000; Lin and Fan, 2004; Kommini et al., 2011; Zhang et al., 2011; Lin et al., 2015), because IR images are independent of illumination and impervious to a shading problem. In addition, IR images provide additional information on the palm, such as the thermal distribution and physiological structure.

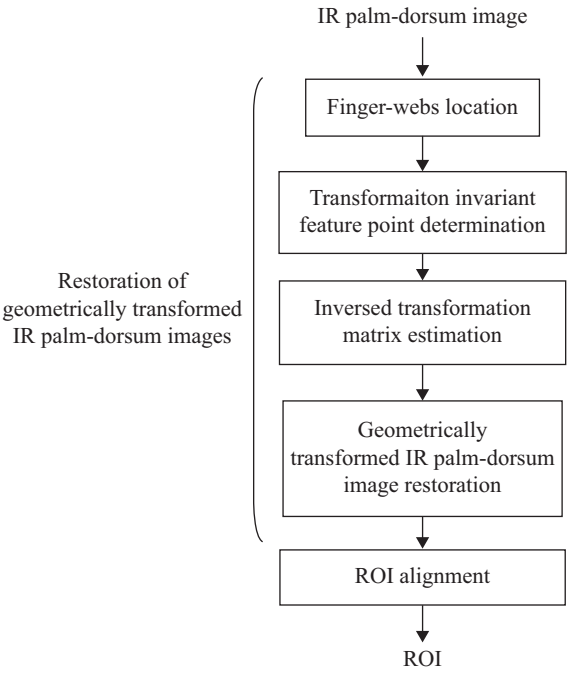

Fig. 2. Block diagram of the proposed approach.

This paper proposes an approach to restoring and aligning ROIs in various IR palm-dorsum images captured in contactless scenarios. Fig. 2 illustrates a block diagram of the proposed approach, which consists of two primary stages: geometrically transformed IR palm-dorsum image restoration, and ROI alignment.

The two-dimensional affine image transformation scheme is applied to estimate the geometric transformation matrix. The geometrically transformed IR palm-dorsum image, based on the inverse of the estimated matrix, is then restored. Finally, the ROI is aligned in the restored IR palm-dorsum images. The security and sanitation concerns are mitigated and the accuracy and user-friendliness are improved when hand-based biometrics are based on the features extracted from the ROI.

The remainder of this paper is organized as follows: Section 2 discusses the restoration scheme for geometrically transformed IR palm-dorsum images that can be used to restore the geometric transformations caused by images captured in contactless scenarios, Section 3 presents the ROI alignment method, and Section 4 presents experimental results to verify the proposed approach. Section 5 concludes the paper.

II. RESTORING GEOMETRICALLY TRANSFORMED INFRARED PALM-DORSUM IMAGES

In hand-based biometrics, the palm is typically placed on a

flat surface to facilitate the acquisition procedure, segmentation, and posterior feature extraction. This situation causes security, sanitation, and user-friendliness concerns. Thus, hand-based biometrics is evolving to contactless scenarios that acquire IR palm-dorsum images in a free space, increasing user acceptability and usability.

However, contactless scenarios cause variation in the distance between the palm and the camera, palm rotation, palm pose, and unconstrained environmental conditions. These variations cause the geometric transformations of IR palm-dorsum images, including translation, rotation, scale and shear, which constitute affine transformations. The biometric system must be invariant to all of these transformations.

Currently, contactless hand-based biometric approaches are increasingly being considered because of their property of user-acceptable sanitation. Previous studies have disregarded the restoration of geometric transformations of IR palm-dorsum images. This paper proposes an approach to resolve this problem.

1. Finger-webs Locating

The procedures (Lin and Fan, 2004; Lin et al., 2005) used to locate the finger-webs are described as follows:

Step 1. Adopt the mode method described in (Sonka et al., 1999) to automatically determine the threshold for segmenting the palm region.
Step 2. Employ the inner border tracing algorithm (Sonka et al., 1999) to locate the palm border.
Step 3. Locate the middle point of the intersection line formed by the wrist and the bottom margin of the IR palm-dorsum image.
Step 4. Compute the Euclidean distance between each border pixel and the wrist middle point. These distances are adopted to construct a distance distribution profile exhibiting a shape similar to the geometric shape of a palm.

Apply wavelet transformation to determine the four local minimums of the distance distribution profile, which are the locations of the four finger-webs.

2. Transformation Invariant Feature Point Determination

All of the control point sets in one IR palm-dorsum image I(x, y) seek their own matched control point set in the other transformed IR palm-dorsum image I(x_t, y_t) for a complete match. The two control point sets can be mapped to the same canonical frame buffer for matching by measuring the distance between them. The control point sets are TIPFs that generate the minimal measuring distance. The distance used in this study was a modified Hausdorff distance (Huttenlocher et al., 1993). Suppose that the control point sets of the two IR palm-dorsum images are already mapped to the canonical frame buffer, I(x, y) and I(x_t, y_t), are $p = \{p_0, \ldots\ldots, p_{M_1-1}\}$ and $p^* = \{p_0^*, \ldots\ldots, p_{M_2-1}^*\}$, respectively. The distance between them is then defined as

$$D(p, p^*) = \max(h(p, p^*), h(p^*, p))$$

$$\text{where } h(p, p^*) = 1/(M_1 d_1) \sum_{i=0}^{M_1-1} p_j^* \in p^* \min \left\| p_i - p_j^* \right\| \quad (1)$$

$$h(p^*, p) = 1/(M_2 d_2) \sum_{i=0}^{M_2-1} p_j \in p \min \left\| p_i^* - p_j \right\|$$

where d_1 is the mean square distance of all the points in control point set p to its geometric center, and d_2 is similarly defined with respect to p^*.

Theoretically, three pairs of control points with known coordinates (three control points on the original image and three control points on the transformed image) can be used to determine the element values of the transformed matrix that is constructed using the coordinates of the three pairs of control points.

Determining the correlative pair of TIFPs from the two IR palm-dorsum images is a crucial and challenging task. By observing the IR palm-dorsum images carefully, finger-webs located at fixed positions in different IR palm-dorsum images can be identified. These finger-webs are highly suitable for use as control points.

The four finger-webs generate $C_3^4 = 4$ different three-point sets. Thus, this study involved adopting the four finger-webs of original and transformed images as control points and applying the Hausdorff distance to determine the three-TIFP set from the four three-point sets that were generated using the four finger-webs. The determined three-TIFP set was applied to estimate the transformation matrix A_e and the inversed transformation matrix A_e^{-1}.

3. Restoration Mechanism of Geometric Transformation

To simplify discussion, the interpolation and round-off error of the transformation were disregarded in the proposed approach. Thus, the proposed approach involves assuming that an original IR palm-dorsum image I(x, y) is related to a transformed IR palm-dorsum image I(x_t, y_t) through a geometric transformation $(x_t, y_t) = f(x, y)$, where (x, y) and (x_t, y_t) are the coordinates of the images. The optimal transformation estimator minimizes the pixel restoration error. Thus, the proposed approach is as follows:

$$\text{minimize} \sum \left\| \mathrm{I}(x_e, y_e) - \mathrm{I}(x_t, y_t) \right\|^2 \quad (2)$$

$$(x_e, y_e, x_t, y_t)$$

where "$\| \bullet \|$" denotes the L_2 norm and (x_e, y_e) denotes the estimated coordinate restoration.

Based on the affine transformation, a point (x, y) is transformed to (x_t, y_t) by using

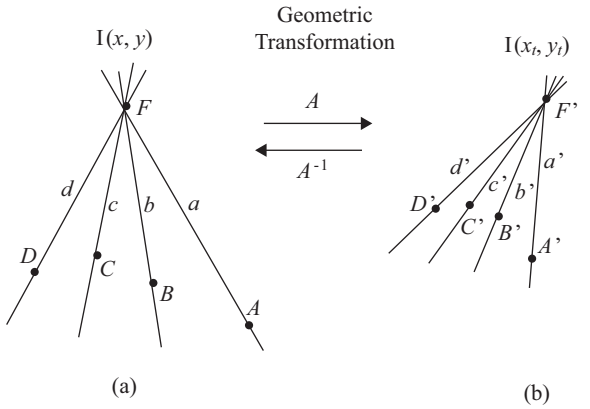

Fig. 3. shows the geometric transformation relationships of I(x, y), I(x_t, y_t), A and A^{-1}. (a) shows the original IR image I(x, y). *B*, *C*, *D*, *E* and *F* are the pixels on I(x, y). *b*, *c*, *d* and *e* represent the distance from *B*, *C*, *D*, *E* to *F*, respectively. (b) shows the geometric transformed IR image I(x_t, y_t). *B'*, *C'*, *D'*, *E'* and *F'* are the pixels on I(x_t, y_t). *b'*, *c'*, *d'* and *e'* represent the distance from *B'*, *C'*, *D'*, *E'* to *F'*, respectively. *A* means the geometric transformation matrix and A^{-1} means the inverse geometric transformation matrix.

$$\begin{aligned}\begin{pmatrix} x_t \\ y_t \end{pmatrix} &= \begin{pmatrix} a_{11} & a_{12} \\ a_{21} & a_{22} \end{pmatrix}\begin{pmatrix} x \\ y \end{pmatrix} + \begin{pmatrix} a_{13} \\ a_{23} \end{pmatrix} \\ &= \begin{pmatrix} \cos\phi & \sin\phi \\ -\sin\phi & \cos\phi \end{pmatrix}\begin{pmatrix} s_x & 0 \\ 0 & s_y \end{pmatrix}\begin{pmatrix} x \\ y \end{pmatrix} + \begin{pmatrix} t_x \\ t_y \end{pmatrix}\end{aligned} \tag{3}$$

where ϕ denotes a rotation angle; s_x and s_y denote x- and y-direction scale, respectively; and t_x and t_y denote x- and y-direction translation, respectively. In homogeneous coordinates, the transformation can be represented by a single matrix A:

$$\begin{aligned}\begin{pmatrix} x_t \\ y_t \\ 1 \end{pmatrix} &= \begin{pmatrix} a_{11} & a_{12} & a_{13} \\ a_{21} & a_{22} & a_{23} \\ 0 & 0 & 1 \end{pmatrix}\begin{pmatrix} x \\ y \\ 1 \end{pmatrix} \\ &= \begin{pmatrix} a_x^T & \\ a_y^T & \\ 0 \quad 0 & 1 \end{pmatrix}\begin{pmatrix} x \\ y \\ 1 \end{pmatrix} = A\begin{pmatrix} x \\ y \\ 1 \end{pmatrix}\end{aligned} \tag{4}$$

where $a_x^T = [a_{11}\ a_{12}\ a_{13}]$ and $a_y^T = [a_{21}\ a_{22}\ a_{23}]$. The relative inverse transformation can be represented as

$$\begin{pmatrix} x \\ y \\ 1 \end{pmatrix} = A^{-1}\begin{pmatrix} x_t \\ y_t \\ 1 \end{pmatrix} = \begin{pmatrix} a_x^{*T} & \\ a_y^{*T} & \\ 0 \quad 0 & 1 \end{pmatrix}\begin{pmatrix} x_t \\ y_t \\ 1 \end{pmatrix} \tag{5}$$

where a_x^* and a_y^* are the first and second rows of the inverse transformation matrix A^{-1}.

Fig. 3 shows the geometric transformation relationships of I(x, y), I(x_t, y_t), A and A^{-1}.

To understand whether two IR palm-dorsum images, I(x, y) and I(x_t, y_t), are affine related, the proposed approach must first determine the specific transformation between them. Assuming that two control point sets represent two affine-related IR palm-dorsum images, the proposed approach attempts to match the two control points. However, the two control point sets are not guaranteed to relate to each other through the same affine transformation. Researchers have yet to be successful in resolving this difficult problem.

In this study, the proposed approach involved the transformation invariant feature point (TIFP) concept to solve this problem. Suppose that the transformation between the control point set I_{cp} in the IR palm-dorsum image I and control point set II_{cp} in the IR palm-dorsum image II is already known; the proposed approach can then match the control points to each other in one IR palm-dorsum image. These matched control points are the TIFPs. If additional control points are used, the probability of selecting precise TIFPs can be increase. Thus, the transformation can be more accurately estimated. In reality, because the transformation is not known in advance, the proposed approach adopts a TIFP selection technique to estimate the TIFPs and geometric transformation parameters, which is described follows.

Suppose that (p_x, p_y) and (p_{tx}, p_{ty}) are the coordinates of control point sets I_{cp} and II_{cp}, respectively. Let (p_{wx}, p_{wy}) denote point set of frame I warped to frame buffer II by using A_e, the estimated transformation matrix, and let (p_{bx}, p_{by}) denote the point set of frame II warped back to frame buffer I by using A_e^{-1}, the inversed matrix of A_e. The proposed approach is as follows:

$$\text{minimize} \left\|p_x - p_{bx}\right\|^2 + \left\|p_y - p_{by}\right\|^2 + \left\|p_{tx} - p_{wx}\right\|^2 + \left\|p_{ty} - p_{wy}\right\|^2 \tag{6}$$

The sum of the first two terms in (6) is the control point matching error in frame buffer I. The sum of the final two terms is the control points matching error in frame buffer II. Because of the interpolation and round-off error, (p_{bx}, p_{by}) does not lie exactly in the sampling grid of frame buffer I, even if A_e^{-1} is accurate. Thus, (p_{bx}, p_{by}) does not coincide with (p_x, p_y). According to the affine invariance property, the minimization of the first two terms and the final two terms in (6) are equivalent. Thus, the proposed approach can only retain the final two terms in (6).

Because the same transformation parameters are used in both frame buffers I and II, the control points (p_{bx}, p_{by}) are related to (p_x, p_y) by using the same affine transformation A_e^{-1}. The transformation parameters can be expressed as

$$\begin{aligned} p_{wx} &= \begin{bmatrix} p_x & p_y & 1 \end{bmatrix} a_{ex}, \quad p_{wy} = \begin{bmatrix} p_x & p_y & 1 \end{bmatrix} a_{ey} \\ p_{bx} &= \begin{bmatrix} p_{tx} & p_{ty} & 1 \end{bmatrix} a_{ex}^*, \quad p_{by} = \begin{bmatrix} p_{tx} & p_{ty} & 1 \end{bmatrix} a_{ey}^* \end{aligned} \tag{7}$$

where a_{ex} and a_{ey} denote the estimated transformation parameters in row vector form, as in (4), and a^*_{ex} and a^*_{ey} denote the inverse of the estimated transformation in row vector form, as in (5).

III. REGION OF INTEREST ALIGNMENT

The geometrically transformed IR palm-dorsum images captured in the contactless scenarios were restored using the aforementioned procedures. In this study, the second and fourth finger-webs were used as the fixed-point references to define the ROI. To define a square ROI, the palm was rotated to let the second (FW_2) and fourth (FW_4) finger-webs be located on the horizon. The second and fourth finger-webs, Fw_2 and Fw_4, were then applied as the fixed-point references to define a square ROI. Define the middle point Fw_m of the line $\overline{FW_2FW_4}$ first. The terms R_1 (upper-left), R_2 (upper-right), R_3 (bottom- right), and R_4 (bottom-left) represented the four corners of the ROI. The top side line $\overline{R_1R_2}$ of the ROI was parallel to the line $\overline{FW_2FW_4}$ at a distance that was half the width of the medius. In addition, the line traversed Fw_m and the middle point of line $\overline{R_1R_2}$ was perpendicular to line $\overline{R_1R_2}$ and $\overline{FW_2FW_4}$. Finally, the original coordinate (0, 0) at the upper-left point R_1 of the ROI was redefined.

The two finger-webs substituted for the fixed pegs, and the approximate, but not absolute, immovable ROI was determined. Thus, the displacement of the ROI was reduced to an acceptable range in IR palm-dorsum images. Consequently, the identification performance was improved.

IV. EXPERIMENTS

The accuracy of IR palm-dorsum image restoration can be measured using the average restoration error ε, which can be expressed as

$$\varepsilon = \left(1/M \times N\right) \sum_x \sum_y \left\| f\left(x_e, y_e\right) - f_e\left(x_t, y_t\right) \right\|^2 \qquad (8)$$

where (x_e, y_e) and (x_t, y_t) denote the coordinates of two IR palm-dorsum images $I(x_e, y_e)$ and $I(x_t, y_t)$, respectively. The IR palm-dorsum image size is $M \times N$ pixels. The two IR palm-dorsum images are related by a geometric transformation f: $(x_t, y_t) = f(x, y)$. Furthermore, f_e is the estimated transformation and ε denotes the average restoration error.

1. Database Collection

To verify the effectiveness and validity of the proposed approach, a database of IR palm-dorsum images was required. A low-resolution IR camera was used to acquire IR palm-dorsum images in contactless scenarios, as illustrated in Fig. 4. The palms do not require fixed pegs or a platform to constrain the palm position while acquiring the IR palm-dorsum images.

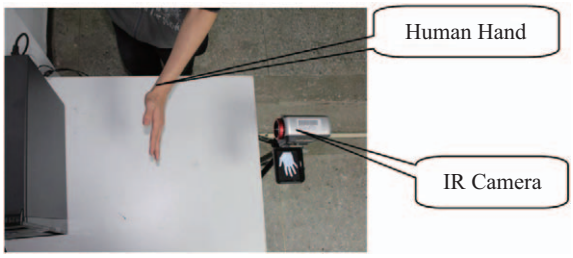

Fig. 4. The IR camera was used to capture the palm-dorsum images in contactless scenarios.

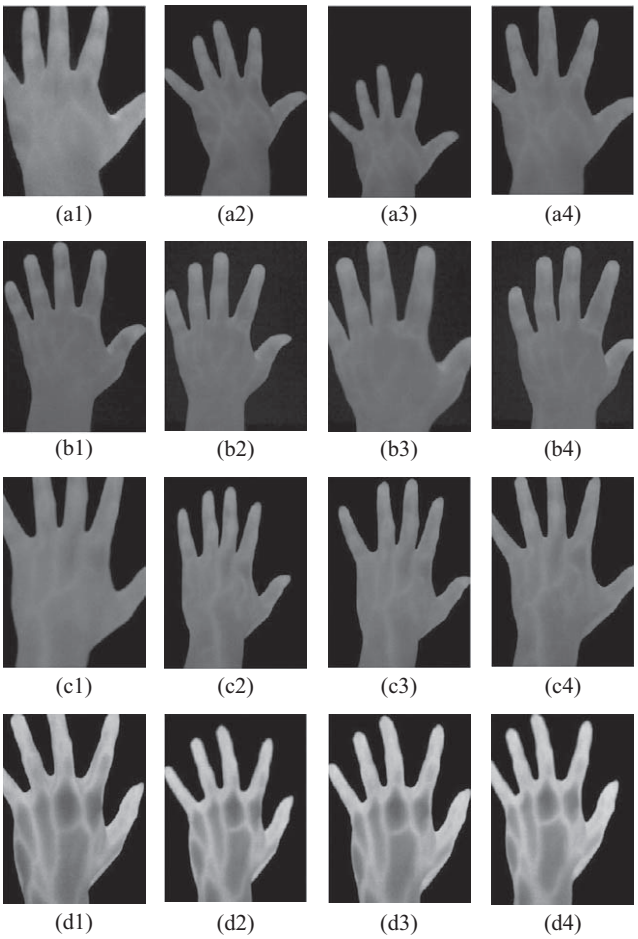

Fig. 5. The 16 IR palm-dorsum images captured using a low-resolution IR camera in contactless scenarios; four IR palm-dorsum images in each row were captured from the same palm-dorsum.

The palms can be posed freely in pose three-dimensional space.

The IR camera applied to capture thermal images is Thermo GEAR G100 that is produced by the NEC Corp. The main specifications of Thermo GEAR G100 described as follows:

Detector: 320 × 240 elements uncooled Focal Plane Array (FPA)
IR wavelength: 8-14 μm
NETD: 0.08°C at 30°C ambient temperature
IFOV: 1.78 mrad

MRT: 0.05°C at 0.5 cycle/mRad
Output: JPEG image format

The platform utilized to evaluate the proposed approach includes an operation system Microsoft Windows XP SP3, a dual core CPU Intel Core (R) E8400 with clock rate 3.0 GHz and a memory module 4 Gbytes DDR2 1333. The display device is the NVIDIA GeForce 8500GT. The program to simulate the approach is developed by Matlab 7.0.

A total of 300 IR palm-dorsum images were captured to form a database. These images were collected from 10 volunteers. For each volunteer, 30 IR palm-dorsum images were captured during three sessions at intervals of at least 1 week. The size of each low-resolution IR palm-dorsum image was 320 × 240 pixels. Each pixel was represented by 256 gray levels. In addition, the IR palm-dorsum images were captured under random lighting conditions. Thus, the database includes the variations of the IR palm-dorsum images under various conditions.

Fig. 5 presents 16 IR palm-dorsum images captured using a low-resolution IR camera in contactless scenarios. Four IR palm-dorsum images in each row were captured from the same palm-dorsum. These images exhibit various geometric transformations, including rotation, scale, translation and shear.

2. Experimental Results

Fig. 5(a1) was used as the original IR palm-dorsum image, and Fig. 6 shows the results of the finger-web location and ROI extraction. Fig. 6(a) shows the histogram of the original IR palm-dorsum image that is illustrated in Fig. 5(a1). The histogram is typically bimodal. The palm-dorsum region can be segmented using the mode method. Fig. 6(b) illustrates the binary palm-dorsum region, which is the original IR palm-dorsum image segmented by the threshold selected using the mode method. The shape of the binary palm-dorsum region satisfactorily matches the original IR palm-dorsum image. Fig. 6(b) indicates that the mode method effectively segmented the palm-dorsum region from the IR palm-dorsum image. Fig. 6(c) indicates that the distance distribution profile was constructed using the Euclidean distance between each border pixel and the wrist middle point *Wm* in sequence. The local minimums in the profile are the locations of finger-webs FW_1-FW_4. These four finger-webs were used as control points in this study. The TIFPs were determined from these control points for estimating the geometric transformation matrix.

3. IR Palm-Dorsum Image Restoration by Using a Known Artificial Transformation Matrix

In this study, geometrically transformed IR palm-dorsum images were artificially generated to evaluate the effectiveness and validity of the proposed approach. These IR palm-dorsum images were generated using the known transformation matrices consisting of known randomly selected transformation parameters. Thus, the estimated geometric transformation matrix A_e can be compared with the known geometric transformation matrix A.

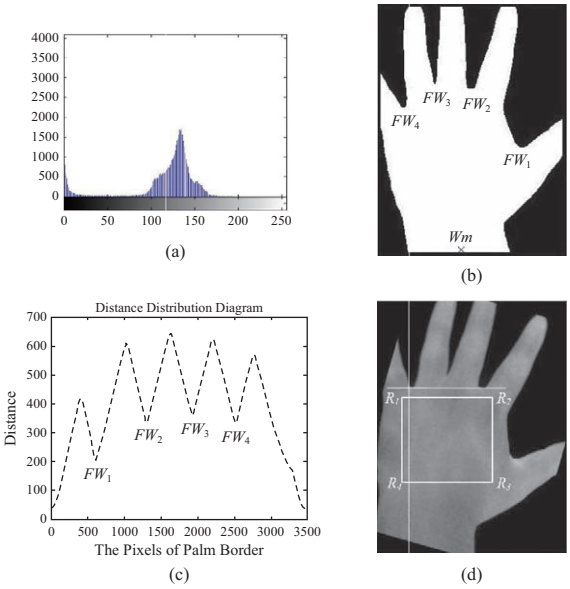

Fig. 6. (a) The histogram of the original IR palm-dorsum image presented in Fig. 5(a1); (b) The palm region segmented using the mode method and transferred to the binary IR palm-dorsum image; (c) The local minimums in this distance distribution profile are the locations of finger-webs FW_1-FW_4; (d) To define a square ROI, rotate the palm to allow the second (FW_2) and fourth (FW_4) finger-webs to be located on the horizon. Apply the second and fourth finger-webs as the fixed-point references to define a square ROI.

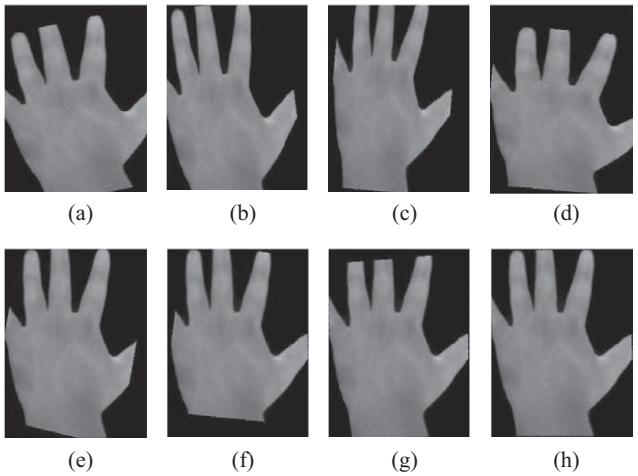

Fig. 7. (a)-(d) The artificial geometrically transformed IR palm-dorsum images of Fig. 5(a1). (e)-(h) The restored IR palm-dorsum images of (a)-(d), respectively.

Fig. 7 presents the results from applying the proposed approach to restore the geometrically transformed IR palm-dorsum images by using known artificial transformation matrices. The original IR palm-dorsum image is illustrated in Fig. 5(a1). The four artificial geometrically transformed IR palm-dorsum images are illustrated in Figs. 7(a)-6(d). Their related randomly selected transformation parameter sets, rotation degree θ, x-direction translation t_x, y-direction translation t_y, x-direction scale factor

Table 1. Artificial transformation matrix A versus estimated transformation matrix A_e, based on Fig. 5(a1).

$$W=\begin{pmatrix}34 & 73 & 118 & 179\\ 133 & 103 & 109 & 181\end{pmatrix}$$

Fig. 7(a) $\theta = 12$ $t_x = 11$ $t_y = 15$ $s_x = 1.1$ $s_y = 0.93$

$$A=\begin{pmatrix}1.076 & 0.193 & 11.000\\ -0.229 & 0.910 & 15.000\\ 0.000 & 0.000 & 1.000\end{pmatrix} \quad A_e=\begin{pmatrix}1.070 & 0.185 & 10.998\\ -0.225 & 0.910 & 15.187\\ 0.000 & 0.000 & 1.000\end{pmatrix} \quad \begin{matrix}AvgErr_x = 0.756\\ AvgErr_y = 0.245\end{matrix}$$

$$FW_T=\begin{pmatrix}34 & 70 & 119 & 198\\ 170 & 133 & 129 & 181\end{pmatrix} \quad FW_R=\begin{pmatrix}34 & 73 & 118 & 179\\ 133 & 103 & 109 & 181\end{pmatrix}$$

Fig. 7(b) $\theta = 7$ $t_x = -13$ $t_y = 16$ $s_x = 0.94$ $s_y = 1.12$

$$A=\begin{pmatrix}0.933 & 0.137 & -13.000\\ -0.115 & 1.112 & 16.000\\ 0.000 & 0.000 & 1.000\end{pmatrix} \quad A_e=\begin{pmatrix}0.933 & 0.141 & -12.987\\ -0.114 & 1.115 & 16.307\\ 0.000 & 0.000 & 1.000\end{pmatrix} \quad \begin{matrix}AvgErr_x = 0.364\\ AvgErr_y = 0.350\end{matrix}$$

$$FW_T=\begin{pmatrix}23 & 55 & 99 & 165\\ 156 & 117 & 120 & 193\end{pmatrix} \quad FW_R=\begin{pmatrix}34 & 73 & 118 & 179\\ 133 & 103 & 109 & 181\end{pmatrix}$$

Fig. 7(c) $\theta = -5$ $t_x = -12$ $t_y = -10$ $s_x = 0.85$ $s_y = 1.05$

$$A=\begin{pmatrix}0.847 & -0.092 & -12.000\\ 0.074 & 1.046 & -10.000\\ 0.000 & 0.000 & 1.000\end{pmatrix} \quad A_e=\begin{pmatrix}0.853 & -0.098 & -11.277\\ 0.083 & 1.041 & -9.756\\ 0.000 & 0.000 & 1.000\end{pmatrix} \quad \begin{matrix}AvgErr_x = 0.842\\ AvgErr_y = 0.677\end{matrix}$$

$$FW_T=\begin{pmatrix}38 & 73 & 112 & 157\\ 115 & 85 & 97 & 177\end{pmatrix} \quad FW_R=\begin{pmatrix}34 & 73 & 118 & 179\\ 133 & 103 & 109 & 181\end{pmatrix}$$

Fig. 7(d) $\theta = -10$ $t_x = 9$ $t_y = -15$ $s_x = 0.9$ $s_y = 0.85$

$$A=\begin{pmatrix}0.866 & -0.148 & 9.000\\ 0.156 & 0.837 & -15.000\\ 0.000 & 0.000 & 1.000\end{pmatrix} \quad A_e=\begin{pmatrix}0.883 & -0.147 & 8.982\\ 0.156 & 0.841 & -14.870\\ 0.000 & 0.000 & 1.000\end{pmatrix} \quad \begin{matrix}AvgErr_x = 0.195\\ AvgErr_y = 0.356\end{matrix}$$

$$FW_T=\begin{pmatrix}57 & 96 & 136 & 178\\ 109 & 88 & 102 & 172\end{pmatrix} \quad FW_R=\begin{pmatrix}34 & 73 & 118 & 179\\ 133 & 103 & 109 & 181\end{pmatrix}$$

s_x, y-direction scale factor s_y, and known artificial transformation matrix A, are listed in Table 1. The terms FW, FW_T, and FW_R are the coordinate vectors of the finger-webs in original, transformed, and restored images, respectively.

$$FW=\begin{bmatrix}fw_4 & fw_3 & fw_2 & fw_1\end{bmatrix} \tag{9}$$

where

$$fw_1=\begin{bmatrix}x_{fw1} & y_{fw1}\end{bmatrix}^T,\ fw_2=\begin{bmatrix}x_{fw2} & y_{fw2}\end{bmatrix}^T,$$

$$fw_3=\begin{bmatrix}x_{fw3} & y_{fw3}\end{bmatrix}^T,\ \text{and}\ fw_1=\begin{bmatrix}x_{fw4} & y_{fw4}\end{bmatrix}^T$$

represent the coordinates of FW_1, FW_2, FW_3, and FW_4, respectively.

The terms FW_T and FW_R are defined similarly to FW.

Figs. 7(e)-6(h) present the results of the restored IR palm-dorsum images. To observe the position of the four finger-webs shown in Figs. 7(e)-6(h) and Fig. 5(a1), they were placed in similar positions.

In addition, Table 1 shows the estimated transformation matrix A_e, the coordinate vector of finger-webs in the original image FW, the coordinate vector of finger-webs in the transformed image FW_T, the coordinate vector of finger-webs in the restored image FW_R, the x-direction average restoration error $AvgErr_x$, and the y-direction average restoration error $AvgErr_y$.

The best case occurred with the restoration error, $AvgErr_x$ = 0.195 pixels and $AvgErr_y$ = 0.356 pixels, when the transformation parameters were selected as θ = -10°, t_x = 9 pixels, t_y = -15 pixels, s_x = 0.90, and s_y = 0.85. The coordinate differences between FW and FW_R are zero pixels and zero pixels in x and y directions, respectively. The known artificial transformation matrix A and the relative estimated transformation matrix A_e were

$$A = \begin{pmatrix} 0.886 & -0.148 & 9.000 \\ 0.156 & 0.837 & -15.000 \\ 0.000 & 0.000 & 1.000 \end{pmatrix}$$

$$A_e = \begin{pmatrix} 0.883 & -0.147 & 8.982 \\ 0.156 & 0.841 & -14.870 \\ 0.000 & 0.000 & 1.000 \end{pmatrix}$$

A minor difference between A and A_e was observed. The inverse transformation matrix, A_e^{-1}, of A_e was applied to restore the artificial transformed IR palm-dorsum image, as shown in Fig. 7(d). The restored IR palm-dorsum image is presented in Fig. 7(h).

When the transformation parameters were selected as θ= -5°, t_x = -12 pixels, and t_y = -10 pixels, s_x = 0.85 and s_y = 1.05 were the worst cases, as shown in Table 1. The known artificial transformation matrix A and the relative estimated transformation matrix A_e were

$$A = \begin{pmatrix} 0.847 & -0.092 & -12.000 \\ 0.074 & 1.046 & -10.000 \\ 0.000 & 0.000 & 1.000 \end{pmatrix}$$

$$A_e = \begin{pmatrix} 0.853 & -0.098 & -11.277 \\ 0.083 & 1.041 & -9.756 \\ 0.000 & 0.000 & 1.000 \end{pmatrix}$$

There is minor difference between A and A_e. The inverse transformation matrix, A_e^{-1}, of A_e was applied to restore the artificial transformed IR palm-dorsum image, as shown in Fig. 7(c). The restored IR palm-dorsum image is presented in Fig. 7(g). No coordinate difference between FW and FW_R was observed. The average restoration errors were 0.842 pixels and 0.677 pixels in the x and y directions, respectively.

The errors were primarily caused by the interpolation, round-off errors of the transformation, and low number of control point sets. Only a few control point sets could be used to select TIFPs in the IR palm-dorsum images. Table 1 lists the restoration errors, which were achieved only by selecting TIFPs from the four control point sets in an IR palm-dorsum image with 320 × 240 pixels, or approximately 0.0052% of the total pixel number. The restored IR palm-dorsum images shown in Figs. 7(e)-6(h) and the test results shown in Table 1 both confirmed the effectiveness and validity of the proposed approach.

4. Real-Life IR Palm-Dorsum Image Restoration

The proposed approach was applied to real-life IR palm-dorsum images captured in contactless scenarios. These real-life IR palm-dorsum images exhibited various geometric transformations, including rotation, scale, translation and shear. The precise transformation matrices were not known in advance. Fig. 8 presents the restored IR palm-dorsum images based on the original (reference) IR palm-dorsum images, as illustrated in the first column of Fig. 5. The positions of the four finger-webs of the IR palm-dorsum images shown in Figs. 8(a1)-8(a3) and Fig. 5(a1) were nearly in the same locations. The regions between the wrist and finger root of the restored IR palm-dorsum images were nearly similar to those of the original IR palm-dorsum images. This observation is similar to that of the other IR palm-dorsum images of the same palm-dorsum, as illustrated in Figs. 8(b1)- 8(b3) and Fig. 5(b1), Figs. 8(c1)-8(c3) and Fig. 5(c1), Figs. 8(d1)-8(d3) and Fig. 5(d1).

Table 2 shows the results of applying the proposed approach to restore the real-life IR palm-dorsum images and shows the estimated transformation matrix A_e and finger-web coordi-

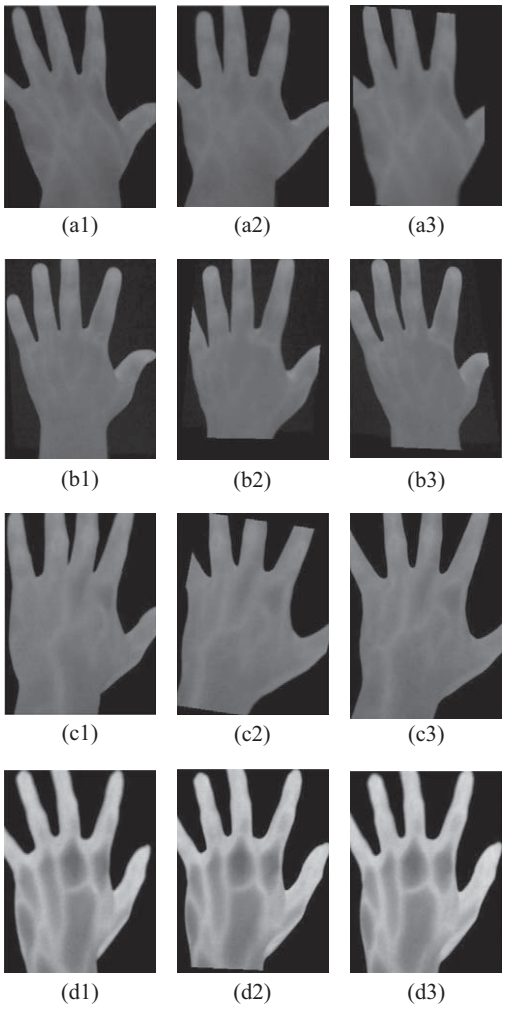

Fig. 8. Restored images of the real-life IR palm-dorsum images shown in Fig. 5. (a1)-(a3) Restored IR palm-dorsum images from Figs. 5(a2)-(a4), (b1)-(b3) Restored IR palm-dorsum images from Figs. 5(b2)-(b4), (c1)-(c3) Restored IR palm-dorsum images from Figs. 5(c2)-(c4), (d1)-(d3) Restored IR palm-dorsum images from Figs. 5(d2)-(d4).

Table 2. Estimated transformation matrix A_e, based on the finger-webs of original and transformed (real-life) images.

Original image		Transformed image (Real-life image)		Estimated transformation matrix	Restored image	
Fig.	Finger-web Coordinates FW	Fig.	Finger-web Coordinates FW_T	A_e	Fig.	Finger-web Coordinates FW_R
5(a1)	$\begin{pmatrix}34 & 73 & 118 & 179\\133 & 103 & 109 & 181\end{pmatrix}$	5(a2)	$\begin{pmatrix}50 & 90 & 136 & 191\\153 & 125 & 130 & 201\end{pmatrix}$	$\begin{pmatrix}1.000 & -0.083 & 13.750\\0.006 & 0.981 & 20.028\\0.000 & 0.000 & 1.000\end{pmatrix}$	8(a1)	$\begin{pmatrix}34 & 71 & 118 & 179\\133 & 104 & 109 & 181\end{pmatrix}$
		5(a3)	$\begin{pmatrix}62 & 91 & 126 & 170\\156 & 130 & 136 & 188\end{pmatrix}$	$\begin{pmatrix}0.754 & -0.028 & 6.096\\-0.026 & 0.744 & 13.887\\0.000 & 0.000 & 1.000\end{pmatrix}$	8(a2)	$\begin{pmatrix}34 & 71 & 118 & 179\\133 & 99 & 109 & 181\end{pmatrix}$
		5(a4)	$\begin{pmatrix}34 & 79 & 131 & 202\\133 & 99 & 97 & 169\end{pmatrix}$	$\begin{pmatrix}1.157 & 0.006 & 13.632\\-0.115 & 1.097 & -7.260\\0.000 & 0.000 & 1.000\end{pmatrix}$	8(a3)	$\begin{pmatrix}34 & 73 & 118 & 179\\133 & 106 & 109 & 181\end{pmatrix}$
5(b1)	$\begin{pmatrix}51 & 85 & 125 & 171\\133 & 116 & 112 & 176\end{pmatrix}$	5(b2)	$\begin{pmatrix}42 & 75 & 111 & 150\\150 & 132 & 129 & 186\end{pmatrix}$	$\begin{pmatrix}0.918 & -0.051 & -16.015\\-0.026 & 0.909 & 12.768\\0.000 & 0.000 & 1.000\end{pmatrix}$	8(b1)	$\begin{pmatrix}51 & 85 & 125 & 171\\133 & 114 & 112 & 176\end{pmatrix}$
		5(b3)	$\begin{pmatrix}37 & 74 & 120 & 180\\165 & 139 & 134 & 202\end{pmatrix}$	$\begin{pmatrix}1.153 & 0.109 & -0.527\\-0.098 & 1.133 & 28.852\\0.000 & 0.000 & 1.000\end{pmatrix}$	8(b2)	$\begin{pmatrix}51 & 85 & 125 & 171\\133 & 113 & 112 & 176\end{pmatrix}$
		5(b4)	$\begin{pmatrix}76 & 113 & 153 & 190\\156 & 136 & 132 & 193\end{pmatrix}$	$\begin{pmatrix}1.001 & -0.141 & 21.229\\-0.045 & 0.985 & 19.517\\0.000 & 0.000 & 1.000\end{pmatrix}$	8(b3)	$\begin{pmatrix}51 & 85 & 125 & 171\\133 & 114 & 112 & 176\end{pmatrix}$
5(c1)	$\begin{pmatrix}52 & 96 & 141 & 188\\102 & 86 & 93 & 190\end{pmatrix}$	5(c2)	$\begin{pmatrix}60 & 94 & 122 & 158\\134 & 115 & 126 & 198\end{pmatrix}$	$\begin{pmatrix}0.700 & 0.032 & -10.552\\-0.014 & 0.749 & 16.488\\0.000 & 0.000 & 1.000\end{pmatrix}$	8(c1)	$\begin{pmatrix}52 & 102 & 141 & 188\\102 & 78 & 93 & 190\end{pmatrix}$
		5(c3)	$\begin{pmatrix}79 & 115 & 148 & 182\\127 & 115 & 121 & 201\end{pmatrix}$	$\begin{pmatrix}0.773 & -0.024 & 10.165\\0.015 & 0.817 & 15.443\\0.000 & 0.000 & 1.000\end{pmatrix}$	8(c2)	$\begin{pmatrix}52 & 98 & 141 & 188\\102 & 86 & 93 & 190\end{pmatrix}$
		5(c4)	$\begin{pmatrix}55 & 91 & 130 & 182\\122 & 103 & 105 & 183\end{pmatrix}$	$\begin{pmatrix}0.855 & 0.122 & 0.205\\-0.105 & 0.855 & 4.467\\0.000 & 0.000 & 1.000\end{pmatrix}$	8(c3)	$\begin{pmatrix}52 & 96 & 141 & 188\\102 & 85 & 93 & 190\end{pmatrix}$
5(d1)	$\begin{pmatrix}39 & 81 & 127 & 171\\133 & 106 & 109 & 189\end{pmatrix}$	5(d2)	$\begin{pmatrix}60 & 95 & 132 & 169\\151 & 129 & 132 & 198\end{pmatrix}$	$\begin{pmatrix}0.821 & 0.011 & 6.806\\0.008 & 0.821 & 13.798\\0.000 & 0.000 & 1.000\end{pmatrix}$	8(d1)	$\begin{pmatrix}39 & 81 & 127 & 171\\133 & 105 & 109 & 189\end{pmatrix}$
		5(d3)	$\begin{pmatrix}60 & 94 & 136 & 180\\150 & 124 & 125 & 199\end{pmatrix}$	$\begin{pmatrix}0.881 & 0.065 & 13.156\\-0.027 & 0.940 & 13.145\\0.000 & 0.000 & 1.000\end{pmatrix}$	8(d2)	$\begin{pmatrix}39 & 80 & 127 & 171\\133 & 106 & 109 & 189\end{pmatrix}$
		5(d4)	$\begin{pmatrix}42 & 75 & 115 & 157\\138 & 112 & 113 & 181\end{pmatrix}$	$\begin{pmatrix}0.846 & 0.060 & -7.872\\-0.046 & 0.875 & -2.057\\0.000 & 0.000 & 1.000\end{pmatrix}$	8(d3)	$\begin{pmatrix}39 & 80 & 127 & 171\\133 & 105 & 109 & 189\end{pmatrix}$

nates of the original, transformed, and restored IR palm-dorsum images. As shown in Table 2, the minimal coordinate differences between FW and FW_R are zero and one pixels, in x and y directions, respectively. The maximal coordinate differences between

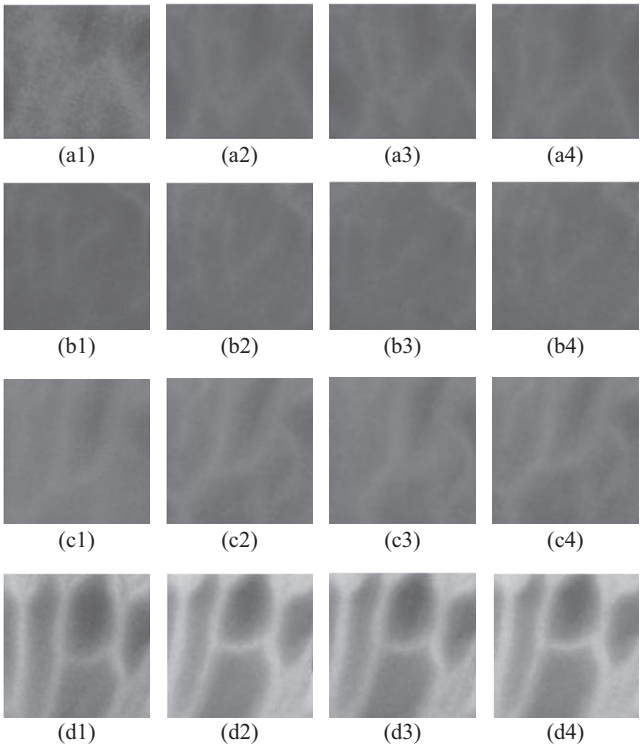

Fig. 9. ROIs extracted from real-life IR palm-dorsum images captured in contactless scenarios and exhibiting geometric transformations, as shown in Figs. 5. (a1)-(a4) ROIs extracted from Figs. 5(a1)-(a4), (b1)-(b4) ROIs extracted from Figs. 5(b1)-(b4), (c1)-(c4) ROIs extracted from Figs. 5(c1)-(c4), (d1)-(d4) ROIs extracted from Figs. 5(d1)-(d4).

FW and FW_R are six and eight pixels, or approximately 2.5% and 2.5% of the entire image, in x and y directions, respectively. These coordinate differences are larger than those shown in Table 1. The large differences are due to the interpolation, round-off errors of the transformation, and low number of control point sets. In addition, the most crucial difference is that the relative coordinates of four finger-webs vary in various real-life IR palmdorsum images captured from the same palm-dorsum.

5. Region of Interest Alignment

The second and fourth finger-webs were applied to the proposed approach as reference fixed-points to align ROIs in the same regions of the IR palm-dorsum images. The ROI size was set at 128 × 128 pixels in this study. Fig. 9 shows the ROIs extracted from the various IR palm-dorsum images of the same palm-dorsum shown in Fig. 5. The ROIs nearly cover the same region on the various IR palm-dorsum images captured from the same palm-dorsum in contactless scenarios.

Figs. 8 and 9 indicate the feasibility and effectiveness of the proposed approach used to restore the real-life IR palm-dorsum images captured in the contactless scenarios that exhibit geometric transformations and to align the ROIs in the same regions in various IR palm-dorsum images.

V. CONCLUSION

This paper proposes an approach for solving a highly challenging problem in the preprocessing of hand-based biometrics. The proposed approach is to restoring IR palm-dorsum images captured in contactless scenarios, and aligning ROIs on the restored IR palm-dorsum images. There are three primary advantages included in the approach. First, the proposed approach incorporates an algorithm to automatically determine the four finger-web locations. Second, geometrically transformed IR palm-dorsum images are restored based on the two-dimensional affine image transformation technique. This technique involves applying the four finger-web locations as control points and using the TIFPs which are selected from the control points to estimate the transformation matrices. In addition, ROIs are aligned in the nearly same region in various IR palm-dorsum images to improve the accuracy of hand-based biometrics based on the features extracted from the ROIs. Finally, no prior knowledge about the IR palm-dorsum images is required and no parameter is required to be manually preset to apply the proposed approach. The experimental results obtained from the experiments on artificial geometrically transformed IR palm-dorsum images as well as real-life IR palm-dorsum images captured in contactless scenarios indicate that the proposed approach is feasible and effective. In addition, this approach can be applied to align ROIs on palmprint images captured in contactless scenarios. Thus, this approach improves accuracy, user-friendliness, security and sanitation and extends the hand-based biometrics for use in security access control systems.

The affine transformation scheme can solve the scale, rotation, translation and shear based on 3 pair invariant feature points. However, there are some limitations of the affine transformation scheme. It could not deal with the project geometric transformation which could be restored by two-dimensional project transformation scheme based on 4 pair invariant feature points. In the future work, the authors will consider taking the 3D information to deal with ROI alignment and cropping.

ACKNOWLEDGMENTS

The authors would like to acknowledge the support for this study through grants from National Chung-Shan Institute of Science & Technology (NCSIST-442-V301 (106)) and Ministry of Science and Technology (MOST 106-2221-E-146-007). They would also thank the anonymous reviewers for their significant and constructive critiques and suggestions, which substantially improved the quality of this paper.

REFERENCES

Cross, J. M. and C. L. Smith (1995). Thermographic imaging of the subcutaneous vascular network of the back of the hand for biometric identification. Proceedings of the IEEE International Carnahan Conference on Security Technology, 20-35.

Dutagaci, H., B. Sankur and E. Yörük (2008). A comparative analysis of global hand appearance-based person recognition. Journal Electronic Imaging 17 (1), 011018/1-011018/19.

Elliott, S., B. Senjaya, E. Kukula, J. Werner and M. Wade (2010). An evaluation

of the human biometric sensor interaction using hand geometry. Proceedings of the IEEE International Carnahan Conference on Security Technology, 259-265.

Huttenlocher, D. P., G. A. Klanderman and W. J. Rucklidge (1993). Comparing images using the hausdorff distance. IEEE Transactions on Pattern Analysis and Machine Intelligence 15 (9), 850-863.

Jain, A. K. and N. Duta (1999). Deformable matching of hand shapes for verification. Proceedings of the International Conference on Image Processing, 857-861.

Jain, A. K., A. Ross and S. Pankanti (1999). A prototype hand geometry based verification system. Proceedings of the International Conference on Audio- and Video-Based Biometric Person Authentication, 166-171.

Jiang, X., W. Xu, L. Sweeney, Y. Li, R. Gross and D. Yurovsky (2007). New directions in contact free hand recognition. Proceedings of the IEEE International Conference on Image Processing, II-389-II-392.

Kommini, C., K. Ellanti and H. Ellanti (2011). Hand dorsal veins and knuckle shape based authentication system. International Journal of Computer Science and Information Technologies 2 (4), 1633-1638.

Kumar, A. and C. Ravikanth (2009). Personal authentication using finger knuckle surface. IEEE Transactions on Information Forensics and Security 4 (1), 98-110.

Lee, J. C. (2012). A novel biometric system based on palm vein image. Pattern Recognition Letters 33(12), 1520-1528.

Lin, C. L. and K. C. Fan (2004). Biometric verification using thermal images of palm-dorsa vein-patterns. IEEE Transactions on Circuits and Systems for Video Technology 14 (2), 199-213.

Lin, C. L., H. Y. Cheng, K. C. Fan, C. W. Lu, C. J. Juan and C. W. Kuo (2013). Bi-feature verification for palmprint images captured in peg-less scenarios. International Journal of Pattern Recognition and Artificial Intelligence 27 (5), 1356007-1-1356007-15.

Lin, C. L., S. H. Wang, H. Y. Cheng, K. C. Fan, W. L. Hsu and C. R. Lai (2015). Bimodal biometric verification using the fusion of palmprint and infrared palm-dorsum vein images. Sensors 15(12), 31339-31361.

Lin, C. L., T. C. Chuang and K. C. Fan (2005). Palmprint verification using hierarchical decomposition. Pattern Recognition 38 (12), 2639-2652.

Morales, A., M. Ferrer, J. Alonso and C. Travieso (2008). Comparing infrared and visible illumination for contactless hand based biometric scheme. Proceedings of the IEEE International Carnahan Conference on Security Technology, 191-197.

Prokoski, F. (2000). History, current status, and future of infrared identification. Proceedings of the IEEE Workshop Computer Vision Beyond Visible Spectrum: Methods and Applications, 5-14.

Raghavendra, R. and C. Busch (2014). Novel image fusion scheme based on dependency measure for robust multispectral palmprint recognition. Pattern Recognition 47 (6), 2205-2221.

Sanchez-Reillo, R., C. Sánchez-Ávila and A. Gonzalez-Macros (2000). Biometric identification through hand geometry measurements. IEEE Transactions on Pattern Analysis and Machine Intelligence 22 (10), 1168-1171.

de-Santos-Sierra, A., C. Sánchez-Ávila, G. Bailador del Pozo and J. Guerra-Casanova (2011). Unconstrained and contactless hand geometry biometrics. Sensors 25, 10143-10164.

Sonka, M., V. Hlavac and R. Boyle (1999). Image Processing, Analysis, and Machine Vision. 2nd ed.; PWS publishing: New York, USA.

Xiong, W., K.A. Toh, W.Y. Yau and X. Jiang (2005). Model-guided deformable hand shape recognition without positioning aids. Pattern Recognition 38(10), 1651-1664.

Yörük, E., E. Konukoglu, B. Sankur and J. Darbon (2006). Shape-based hand recognition. IEEE Transactions on Image Processing 15 (7), 1803-1815.

Zhang, D., Z. Guo, G. Lu, L. Zhang, Y. Liu and W. Zuo (2011). Online joint palmprint and palmvein verification. Expert Systems with Applications 38(3), 2621-2631.

Zheng, G., C. J. Wang and T. Boult (2007). Application of projective invariants in hand geometry biometrics. IEEE Transactions on Information Forensics and Security 2(4), 758-768.

Zhou, Y. and A. Kumar (2011). Human identification using palm-vein images. IEEE Transactions on Information Forensics and Security 6(4), 1259-1274.